INTERFACE

royalsocietypublishing.org/journal/rsif

Research

Cite this article: Dollet B, Louf J-F, Alonzo M, Jensen KH, Marmottant P. 2019 Drying of channels by evaporation through a permeable medium. *J. R. Soc. Interface* **16**: 20180690.
http://dx.doi.org/10.1098/rsif.2018.0690

Received: 14 September 2018
Accepted: 28 January 2019

Subject Category:
Life Sciences–Physics interface

Subject Areas:
biomimetics

Keywords:
drying, pervaporation, leaf, diffusion, biomimetic

Author for correspondence:
Benjamin Dollet
e-mail: benjamin.dollet@univ-grenoble-alpes.fr

Drying of channels by evaporation through a permeable medium

Benjamin Dollet[1], Jean-François Louf[1,2], Mathieu Alonzo[1], Kaare H. Jensen[2] and Philippe Marmottant[1]

[1]Univ. Grenoble Alpes, CNRS, LIPhy, 38000 Grenoble, France
[2]Department of Physics, Technical University of Denmark, 2800 Kgs. Lyngby, Denmark

BD, 0000-0002-1756-7543; KHJ, 0000-0003-0787-5283

We study the drying of isolated channels initially filled with water moulded in a water-permeable polymer (polydimethylsiloxane, PDMS) by pervaporation, when placed in a dry atmosphere. Channel drying is monitored by tracking a meniscus, separating water from air, advancing within the channels. The role of two geometrical parameters, the channel width and the PDMS thickness, is investigated experimentally. All data show that drying displays a truncated exponential dynamics. A fully predictive analytical model, in excellent agreement with the data, is proposed to explain such a dynamics, by solving water diffusion both in the PDMS layer and in the gas inside the channel. This drying process is crucial in geological or biological systems, such as rock disintegration or the drying of plant leaves after cavitation and embolism formation.

1. Introduction

The process of drying is the removal of liquids by evaporation from a solid. It is important in both natural and man-made systems. Chemical separation, which includes drying and distillation, accounts for 10–15% of the world's total energy consumption [1]. Drying is also involved in numerous geological and biological processes, e.g. in rock disintegration [2] or salt weathering [3] by subflorescence growth of salt crystals in drying rocks, or in the drying of soils, an economically important agricultural process [4]. In living organisms, drying is involved in, for example, the regulation of body temperature [5] and nutrient transport in biofilms [6]. Moreover, it is highly important in plants, which can be strongly affected by drought-induced embolism formation, a growing threat in the context of global warming [7].

A common feature of the aforementioned examples is that drying occurs by evaporation from a porous material into the atmosphere, a process known as pervaporation. The microstructure of these materials can be highly complex, and the drying rates are strongly dependent on the specific geometry. However, the underlying structure is often a network of either approximately circular pores or long and linear channels. The drying of porous materials with circular pores is relatively well understood [8]; however, the physical effects and parameters that determine the rate of drying from porous media composed of linear channels are still poorly understood.

For instance, in plant leaves, water flows in tiny parallel conduits located in the xylem tissue of the leaf veins. In normal physiological conditions, incoming water diffuses out of the veins and evaporates at the leaf surface. The catastrophic drying of the channels starts after cavitation events, that is the nucleation of bubbles in water. Cavitation occurs during drought when evaporation results in relatively strong negative pressures. Even if numerous studies have investigated the physical process at the origin of cavitation [9–14], the physical dynamics of its spreading remains elusive.

Here, we propose to explore a simple physical model of linear channels in porous material. We are inspired by a set-up proposed by [9,15–17] to mimic water networks in a leaf, using microfluidic devices made in a porous elastomer. Long linear channels can be found in grass plants for instance (figure 1). In other

THE ROYAL SOCIETY PUBLISHING

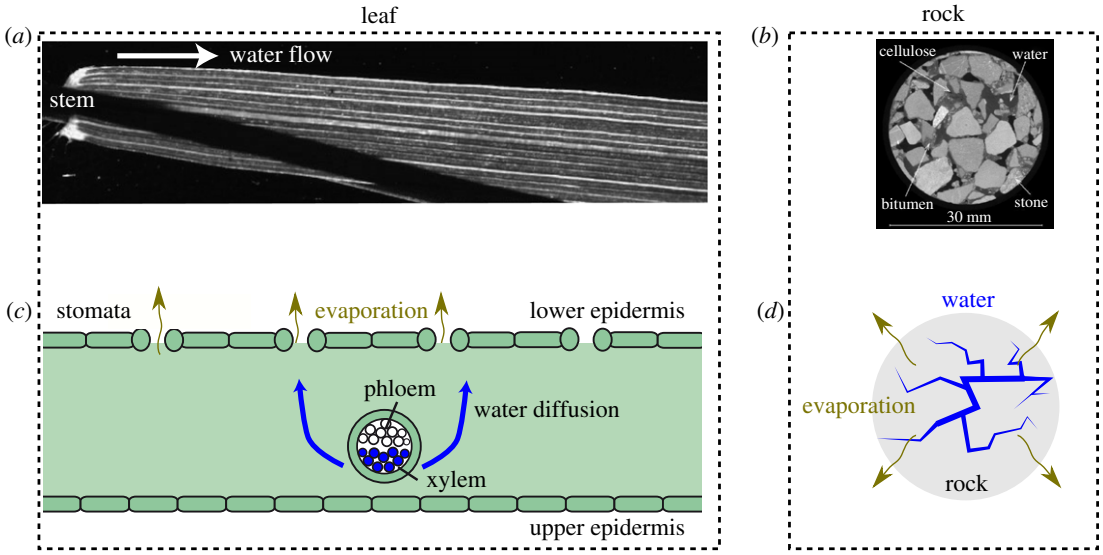

Figure 1. (*a*) Example of linear water conduits in a porous material: a grass leaf. This photograph is turned horizontally, showing parallel veins conducting water from the base of the leaf (here on the left) to the tip. Photograph from the authors, taken in T. Brodribb's laboratory. (*b*) Slice image (from [18]) of computed tomography-scan of wet asphalt sample: water is in all the stone interstices. (*c*) Cross-sectional diagram of water transport in a leaf, here upside-down. The water diffuses from the xylem conduits to the lower epidermis, where the stomata chambers are spread. (*d*) Sketch of a wet rock. Water can evaporate from the water-filled cracks. (Online version in colour.)

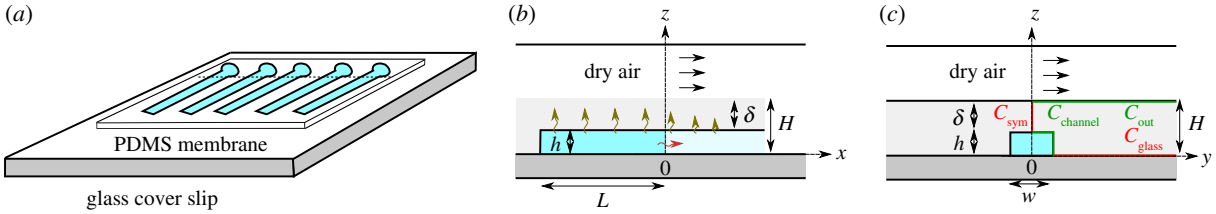

Figure 2. (*a*) Sketch of the experiment inspired by Noblin *et al*. [15]. PDMS channels filled with water (in blue) are opened along the dashed line and submitted to a flow of dry air, subsequently resulting in the evaporation of water from the channels. (*b*) Sketch of a channel longitudinal cross section. The part of the channel filled with water is represented in dark blue, and the one filled with gas in light blue. The green arrows represent the water flux through PDMS, while the red one shows the water flux at the water/air interface. (*c*) Sketch of the transverse cross section of the channels. Water in the channels is represented in blue. In (*b*,*c*), the glass slide is represented in dark grey and the PDMS in light grey. (Online version in colour.)

contexts, this very configuration was also designed in microfluidic devices where pervaporation was used in a chemical engineering context to homogeneously concentrate liquid solutions [19–24]. We therefore hope the present study to be useful for microfluidic applications involving evaporation.

The process of drying of these channels involves a gas/liquid meniscus that is moving as the liquid is diffusing out of the system (similar to [25] or [26]). The main goal of the paper is to measure and predict the evaporative rate of the liquid through polydimethylsiloxane (PDMS) from linear channels having a rectangular cross section, and thus predict the motion of the meniscus.

2. Material and methods

We first describe the fabrication of the microfluidic channels on the top of a glass plate and the drying method.

2.1. Materials

We made channels of width $w = 75$, 100, 125, 150 and 175 µm side by side, separated by a distance of 2.5 mm (figure 2*a*). This distance is small enough that the five channels can be simultaneously imaged, but large enough that diffusive interactions between channels be negligible [15]. The channels were moulded in PDMS using standard soft lithography techniques. Briefly, we first created a mould in a photoresistive material (SU8) on a silicon wafer. We mixed liquid PDMS (Sylgard 184, Dow Corning) with a curing agent in mass proportions 9:1. This mixture was degassed then spin coated on the mould, to create an imprint of controlled thickness, and baked at 65°C for one hour to reticulate the PDMS. This imprint was then bonded to a glass slide. We measured the channel thickness h using an interferometer, and the PDMS thickness H by microscope imaging. The channel thickness was kept at $h = 35 \pm 1$ µm, and experiments were performed for four values of PDMS thickness: $H = 75$, 102, 140 and 249 µm (table 1), within 1 day after channel

Table 1. Set of thicknesses h of the channels and H of the PDMS used in this study, and corresponding symbols in figures 4–7.

symbol	h (µm)	H (µm)
+	35	75
*	37	102
×	37	140
▷	37	249

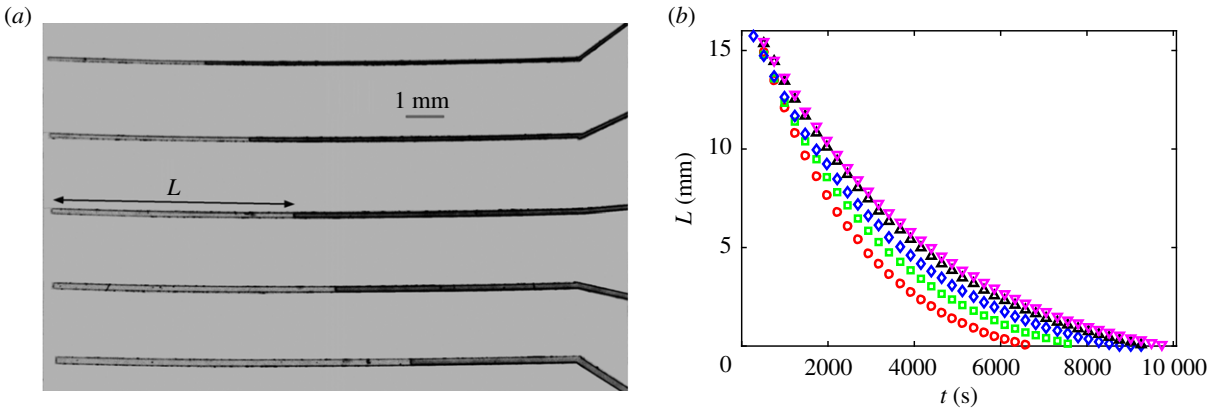

Figure 3. Drying dynamics. (*a*) Micrograph showing the channels, of width $w = 75$, 100, 125, 150 and 175 µm from top to bottom. The bright water-filled part of the channels, of length $L(t)$, is separated from the darker air-filled part by a meniscus which moves from right to left as the channels dry. (*b*) Measurement of $L(t)$ for $h = 37$ µm and $H = 140$ µm (circle: $w = 75$ µm, square: $w = 100$ µm, diamond: $w = 125$ µm, triangle: $w = 150$ µm, inverted triangle: $w = 175$ µm). (Online version in colour.)

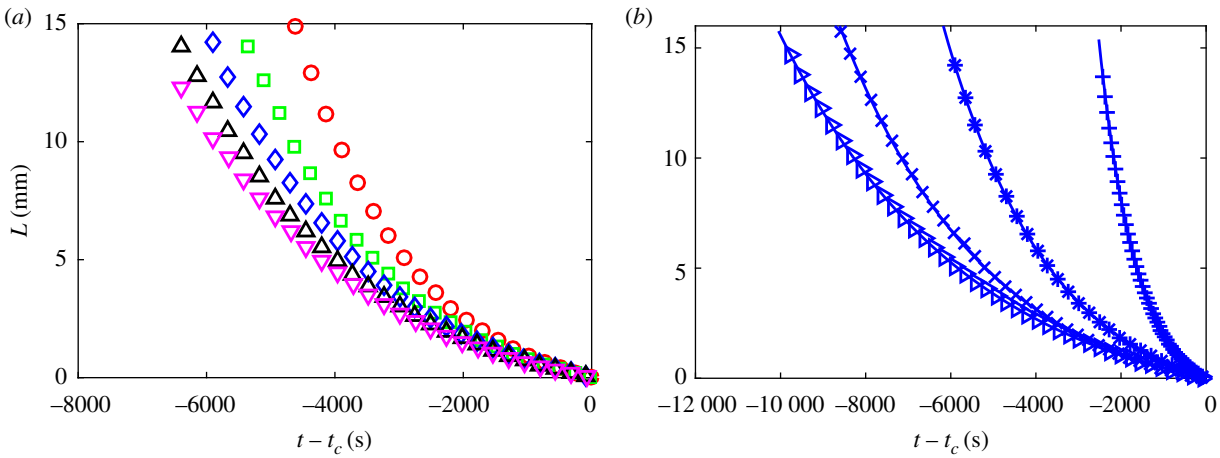

Figure 4. Plot of $L(t - t_c)$. (*a*) The PDMS thickness is fixed (here, $H = 102$ µm) and different colours and symbols represent different channel widths: $w = 75$ µm (circle, red), 100 µm (square, green), 125 µm (diamond, blue), 150 µm (triangle, black) and 175 µm (inverted triangle, magenta). (*b*) The channel width is fixed (here, $w = 125$ µm) and different symbols represent different PDMS thickness H (see table 1 for their definitions). Curves are fitted by equation (4.8), with L_g, L_0 and τ as fitting parameters. (Online version in colour.)

fabrication. Note that this configuration of a porous material on top of impermeable glass closely mimics a leaf whose upper side is covered with impermeable cuticle (figure 1).

2.2. Methods

We opened the channels by manually cutting through the PDMS layer with a scalpel at the junction between the channels and the round part (figure 2*a*). The opening simulates the rupture of the water column by a cavitation bubble in a leaf. To fill the channels with water, we immersed them in deionized water inside a beaker, placed in a vacuum pump for one hour. Once they were water filled, we placed them under dry atmosphere, as follows. We covered them with a Petri dish coverslip pierced by a hole in which a tube is glued, and we flowed through this tube compressed dry air from a bottle (Air Liquide) at a constant flux of 50 ml min^{-1}. This constant circulation along the channel surface ensured that dry conditions were met at the outer surface of PDMS. Each channel progressively dried out, as a meniscus separating water from gas advanced downstream through the channel (figure 3), until reaching the closed end.

The channels were placed under a stereo-microscope objective (Zeiss DV8), and the meniscus motion was imaged with a CCD camera (Allied Visions Technologies, model Pike F-421B, 2000 × 2000 pixels), and recorded by performing a reslice operation along the mid-curve of each channel using ImageJ freeware. We deduced from this process a measurement of $L(t)$, L being the channel length filled with water and t the time, counted from the beginning of the movie.

3. Results

Our experiments characterized the drying of a long channel embedded in a permeable medium. Typical results of these experiments are shown in figure 3*b*. In all our experiments, the length of remaining water $L(t)$ decreases with time t, consistently with the drying process. Interestingly, the drying velocity $|\dot{L}(t)|$ decreases with time as well. Liquid water completely disappears in the channel after a finite time t_c.

To compare different channels more easily, we plot the data as $L(t - t_c)$ in figure 4, such that all curves pass through the origin corresponding to full drying. Figure 4*a* shows results for a given PDMS thickness, but for different channel widths. Here, we can clearly see the influence of the channel width on the drying process: at given PDMS thickness H, the lower the channel width w, the faster the drying process.

Figure 4*b* shows results for a given channel width, but for different PDMS thicknesses. Such a representation clearly shows the influence of the PDMS thickness on the drying process: at given channel width, the lower the PDMS thickness, the faster the drying process.

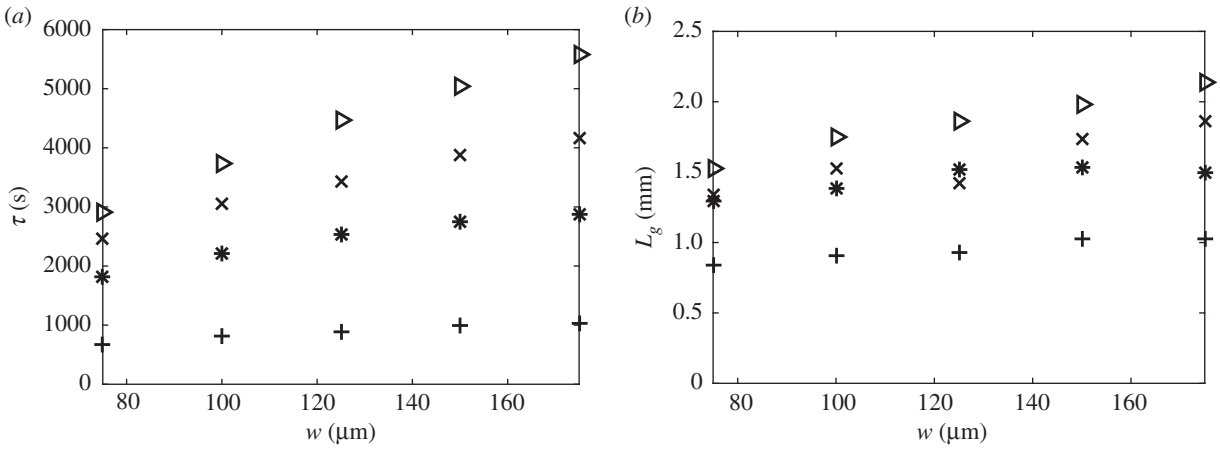

Figure 5. Plot of (*a*) τ and (*b*) L_g as functions of w. See table 1 for the definition of symbols.

4. Theory

In this section, we propose a model to predict the drying dynamics observed in our experiments. The main predictions are summarized at the beginning of §4.4, and they are compared to the experimental data in §5.

4.1. General considerations

We use the following assumptions. (i) As stated in §2, we consider each channel as isolated. (ii) We neglect the entrance effect at the open end of the channel. (iii) We neglect the curvature of the meniscus. (iv) We neglect all pressure variations. (v) We neglect PDMS deformation, and thus assume that the channel is of constant cross section.

We adopt the following coordinates (figure 2*b*,*c*): we fix the origin at the contact line between the meniscus and the glass slide, midway between the two vertical channel walls. Hence, the origin moves at velocity $\dot{L}(t)$ in the laboratory frame. The axis y goes spanwise along the glass slide, the axis x is perpendicular to the meniscus away from the water phase, and the axis z goes upwards away from the glass slide. Hence, the channel cross section is such that $-w/2 \le y \le w/2$ and $0 \le z \le h$, the water phase is at $-L(t) \le x \le 0$, and the gas phase at the other side of the meniscus is at $x > 0$. As we neglect any entrance effect, we do not consider any upper bound on x in the gas phase.

As the volume of water in the channel equals $hwL(t)$, the drying dynamics obeys the conservation equation

$$\frac{\rho}{M} hw\dot{L} = -Q, \tag{4.1}$$

where $\rho = 10^3\,\mathrm{kg\,m^{-3}}$ is the density of liquid water, $M = 1.8 \times 10^{-2}\,\mathrm{kg\,mol^{-1}}$ its molar mass and Q the molar flux of water leaving the water-filled part of the channel. Water diffuses through PDMS with a diffusion coefficient D_P of order $10^{-9}\,\mathrm{m^2\,s^{-1}}$ [15,27,28], whence a diffusive flux given by Fick's Law: $\mathbf{J}_P = -D_P \nabla c_P$, where c_P denotes the water molar concentration field in PDMS. Water vapour diffuses in air with a diffusion coefficient $D_a = 2.8 \times 10^{-5}\,\mathrm{m^2\,s^{-1}}$, and the corresponding Fick's Law is written: $\mathbf{J}_a = -D_a \nabla c_a$, where c_a denotes the water vapour molar concentration field in air. The flux Q can be split in two contributions: one from the water/PDMS interface $\mathcal{S}_\ell$, and one from the meniscus

$$Q = Q_\ell + Q_g,$$

where

$$Q_\ell = \int_{\mathcal{S}_\ell} \mathbf{J}_P \cdot \mathbf{n}\, \mathrm{d}S, \tag{4.2}$$

with $\mathbf{n}$ the outwards normal vector along $\mathcal{S}_\ell$, and

$$Q_g = \int_{-w/2}^{w/2} \mathrm{d}y \int_0^h \mathrm{d}z\, J_{a,z}|_{x=0}. \tag{4.3}$$

As the typical length of the water-filled part (1 cm) is much larger than the typical sizes of the cross section of the channel and of the PDMS (w, h and H are of order 10^2 μm), except at the very end of the drying process, we may in the first approximation assume that in the water-filled part, the problem is invariant by translation along x; this amounts to neglecting edge effects at the closed end of the channel. Therefore, the concentration field c_P is independent of x for $-L \le x \le 0$, and

$$Q_\ell = q_\ell L,$$

with

$$q_\ell = \int_0^h (J_{P,y}|_{y=w/2} - J_{P,y}|_{y=-w/2})\, \mathrm{d}z + \int_{-w/2}^{w/2} J_{P,z}|_{z=h}\, \mathrm{d}y. \tag{4.4}$$

Hence, $Q = q_\ell L + Q_g$. Inserting in (4.1) yields

$$\dot{L} = -\frac{L + L_g}{\tau}, \tag{4.5}$$

with

$$\tau = \frac{\rho h w}{M q_\ell} \tag{4.6}$$

and

$$L_g = \frac{Q_g}{q_\ell}. \tag{4.7}$$

The drying dynamics is thus predicted to follow a truncated exponential law of the form

$$L(t) = (L_0 + L_g)\, \mathrm{e}^{-t/\tau} - L_g, \tag{4.8}$$

where $L_0 = L(t = 0)$ is the initial wet length. Such a law is indeed an excellent fit of the experiments, almost indistinguishable from the data (figure 4). The fitting parameters L_g and τ are plotted as functions of w for the different thicknesses in figure 5*a*,*b*. These plots show the following trends. At fixed H, both τ and L_g increase with increasing w,

consistent with figure 4. This increase is relatively stronger for τ than for L_g. Next, at fixed w and h, both τ and L_g increase with increasing w. Here again, this increase is relatively stronger for τ than for L_g.

The next modelling step consists in predicting q_ℓ (§4.2) and Q_g (§4.3).

4.2. Liquid phase transport q_ℓ

To predict q_ℓ, we have to determine the concentration field of water in PDMS, which obeys the diffusion equation. Note first that as w, h and H are of order $a = 10^{-4}$ m, the diffusion time scale a^2/D_P is of order 10 s, which is much shorter than the experimental time scale of drying, of order 10^4 s from figure 4. Therefore, we may solve a two-dimensional steady diffusion problem, i.e. the two-dimensional Laplace equation

$$\frac{\partial^2 c_P}{\partial y^2} + \frac{\partial^2 c_P}{\partial z^2} = 0. \tag{4.9}$$

As a property of Laplace equation, flux is conserved and we may compute q_ℓ all along the air/PDMS interface, replacing (4.4) by

$$q_\ell = -2D_P \int_0^\infty \left.\frac{\partial c_P}{\partial z}\right|_{z=H} \mathrm{d}y, \tag{4.10}$$

where Fick's Law was used, as well as the symmetry of the problem with respect to the axis $y = 0$.

The boundary conditions are as follows. First, $c_P = c_P^{\mathrm{sat}}$ at the channel/PDMS interface $\mathcal{C}_{\mathrm{channel}}$, which is constituted by the two segments $0 \le y \le w/2$ for $z = h$, and $0 \le z \le h$ for $y = w/2$. The quantity c_P^{sat} is the equilibrium concentration of water in PDMS in contact with water. Second, $\partial c_P/\partial y = 0$ at the symmetry axis $\mathcal{C}_{\mathrm{sym}}$, located at $h \le z \le H$ for $y = 0$. Third, $\partial c_P/\partial z = 0$ at the glass/PDMS interface $\mathcal{C}_{\mathrm{glass}}$, located at $y \ge w/2$ for $z = 0$, because glass is impermeable to water. We refer to figure 2*c* for a sketch of $\mathcal{C}_{\mathrm{channel}}$, $\mathcal{C}_{\mathrm{sym}}$ and $\mathcal{C}_{\mathrm{glass}}$.

Another boundary condition relates the concentration across the PDMS/outer air interface $\mathcal{C}_{\mathrm{out}}$ (figure 2*c*). To write it, we use the study by Harley *et al.* [29], who studied the uptake of water by PDMS in contact with air at various humidities. Their results show small non-ideal behaviours at small and large humidities, but overall the water concentration in PDMS and the humidity are almost proportional. We will thus simply apply Henry's Law on $\mathcal{C}_{\mathrm{out}}$

$$c_a^{\mathrm{out}} = \alpha c_P, \tag{4.11}$$

with c_a^{out} the concentration of water vapour in the ambient atmosphere (in our experiments, we assume that due to the constant circulation of dry air around the channels, $c_a^{\mathrm{out}} = 0$), and α a dimensionless Henry constant. Harley *et al.* [29] measured a concentration of 0.9 cm^3 of water vapour per gram of PDMS in equilibrium with saturated air at 30°C. With a PDMS density $\rho_{\mathrm{PDMS}} = 965\ \mathrm{kg\,m^{-3}}$, this corresponds to a concentration of water in PDMS equal to 36 mol m^{-3}. This value is close to the value of $c_P^{\mathrm{sat}} = 40\ \mathrm{mol\,m^{-3}}$ reported by Randall & Doyle [28]. Moreover, the molar concentration of water in saturated air equals $c_a^{\mathrm{sat}} = p_{\mathrm{sat}}/RT$, with p_{sat} the water vapour pressure in saturated air, R the ideal gas constant and T the temperature. With $p_{\mathrm{sat}} = 3$ kPa, we estimate $c_a^{\mathrm{sat}} = 1\ \mathrm{mol\,m^{-3}}$. Hence, we simply estimate α as $\alpha = c_a^{\mathrm{sat}}/c_P^{\mathrm{sat}} = 0.03$.

Finally, as coupling between channels is neglected, c_P equilibrates with the outer atmosphere far from the channel: $\lim_{y\to\infty} \alpha c_P = c_a^{\mathrm{out}}$, from Henry's Law (4.11).

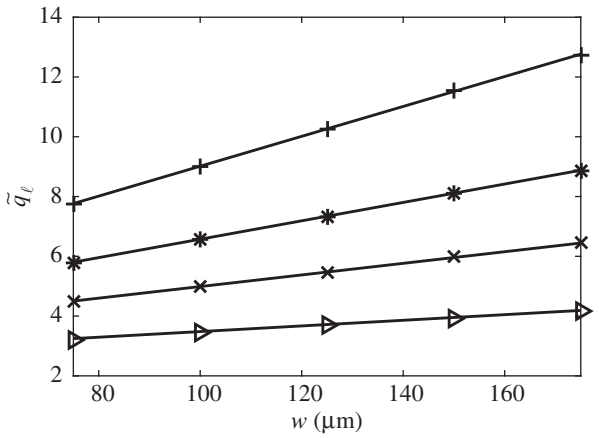

Figure 6. Plot of the dimensionless flux $\tilde{q}_\ell$ as a function of w, for different values of H (see table 1 for the definition of symbols). Symbols come from the numerical resolution of equations (A 6) and (A 13) of the exact model. The lines come from the simplified prediction (4.13) for the flux, which turns out to be an excellent approximation.

We solve this problem analytically using conformal mapping techniques. The full derivation is given in appendix A. It is exact, and the numerical resolution of (A 6) and (A 13) provides the exact value of the flux for arbitrary values of h, w and H. In particular, we derive an explicit simplified prediction of the flux as a function of the geometrical parameters. The dimensionless evaporative flux $\tilde{q}_\ell$ is defined as

$$q_\ell = D_P\left(c_P^{\mathrm{sat}} - \frac{c_a^{\mathrm{out}}}{\alpha}\right)\tilde{q}_\ell = D_P c_P^{\mathrm{sat}}(1 - \mathrm{RH})\tilde{q}_\ell, \tag{4.12}$$

where $\mathrm{RH} = c_a^{\mathrm{out}}/c_a^{\mathrm{sat}}$ is the relative humidity of the ambient air, and we predict

$$\tilde{q}_\ell \simeq \frac{w}{\delta} + \frac{2}{\pi}\left[\ln\frac{(H+\delta)h}{\delta^2} + \frac{H}{\delta}\ln\frac{H+\delta}{h}\right]. \tag{4.13}$$

This approximated expression is seen to fit the exact numerical values of the flux within less than 1% (figure 6). The range of validity of (4.13) is further discussed in appendix A (figure 11). This excellent agreement fully justifies the interest of the analytical approach, which yields the explicit dependence of the flux on all geometrical parameters.

4.3. Gas phase transport Q_g

The second contribution to drying, Q_g, arises from the exchanges in the region $x > 0$ above the channel filled with gas. Physically, the gas close to the meniscus is still saturated with water vapour, then it dries out through pervaporation of water from the channel inside to the outer dry atmosphere through PDMS. Hence, the problem is much more difficult than in §4.2, for the following reasons. (i) It becomes dependent on x and therefore fully three dimensional. (ii) It couples diffusion in two media: in the PDMS, and in the gas within the channel. As the latter phase is a fluid, convection effects must, in principle, be accounted for. However, the meniscus velocity does not exceed 20 μm s^{-1} (figure 4). Hence, with channel dimensions of order 10^{-4} m, the Péclet number $Pe = \dot{L}h/D_a$ comparing convection and diffusion remains of order 10^{-4}, hence convection remains negligible. (iii) In principle, as $\dot{L}(t)$ varies with time, the problem is time dependent. Nevertheless, we will consider that the problem is steady in the frame of the moving meniscus.

In the frame of these approximations, we have to solve for $y > 0$ two steady three-dimensional diffusion problems, one for the concentration field c_P in the PDMS, and one for the concentration field c_a in the channel. These two fields obey the three-dimensional Laplace equation

$$\frac{\partial^2 c_i}{\partial x^2} + \frac{\partial^2 c_i}{\partial y^2} + \frac{\partial^2 c_i}{\partial z^2} = 0, \tag{4.14}$$

for $i = a$ and P. The boundary conditions are as follows. Like before, we have the condition on $\mathcal{C}_{\text{out}}$: $c_P = c_a^{\text{out}}/\alpha$, the no-flux conditions at the glass surface: $\partial c_P/\partial z = 0$ at $y \geq w/2$, and $\partial c_a/\partial z = 0$ at $0 \leq y \leq w/2$, for $z = 0$, and the symmetry conditions: $\partial c_P/\partial y = 0$ at $h \leq z \leq H$ and $\partial c_a/\partial y = 0$ at $0 \leq z \leq h$, for $y = 0$. On $\mathcal{C}_{\text{channel}}$, we now have to apply the continuity of fluxes: $D_a \nabla c_a \cdot \mathbf{n} = D_P \nabla c_P \cdot \mathbf{n}$, where $\mathbf{n}$ is the unit normal vector on $\mathcal{C}_{\text{channel}}$, and Henry's Law (4.11) on the form: $c_a = \alpha c_P$. Finally, far away from the meniscus, the channel and PDMS are equilibrated with the ambient atmosphere: $\lim_{x\to\infty} c_a = \lim_{x\to\infty} \alpha c_P = c_a^{\text{out}}$.

Despite its complexity, we solve this problem analytically, using a perturbation scheme based on the fact that $D_P/D_a \ll 1$. The full derivation is given in appendix B. Its final outcome is the prediction of the flux Q_g

$$Q_g = c_P^{\text{sat}}(1 - \text{RH})\sqrt{\alpha D_a D_P h w \tilde{q}_\ell}. \tag{4.15}$$

4.4. Prediction for the dynamics of drying

To summarize the theoretical analysis and facilitate the comparison with data, we recall that the drying equation is (4.5): $\dot{L} = -(L + L_g)/\tau$, with, from (4.5), (4.6) and (4.12),

$$\tau = \frac{\rho h w}{D_P M c_P^{\text{sat}}(1 - \text{RH})\tilde{q}_\ell}, \tag{4.16}$$

and from (4.7), (4.12) and (4.15),

$$L_g = \sqrt{\frac{\alpha D_a h w}{D_P \tilde{q}_\ell}}, \tag{4.17}$$

where we recall the definition of the various quantities: $\rho = 10^3\,\text{kg m}^{-3}$ is the water density, $M = 0.018\,\text{kg mol}^{-1}$ its molar mass, h the channel height, w its width, D_P and D_a are the diffusion coefficients of water, respectively, in PDMS and in air, c_P^{sat} and c_a^{out} are, respectively, the saturation concentration of water vapour in air and its concentration in the air surrounding the PDMS chip, $\alpha = 0.03$ is the Henry constant quantifying the balance of water concentration at the air/PDMS interface; see (4.11). Finally, $\tilde{q}_\ell$ is the dimensionless flux of water per unit channel length, of which (4.13) is a convenient approximation.

It is worth noting that L_g is the characteristic distance from the meniscus over which air dries in the channel; see (B 13). We note also that the combination L_g^2/τ is predicted to be independent from $\tilde{q}_\ell$ and thus from geometrical parameters

$$\frac{L_g^2}{\tau} = \alpha D_a \frac{M}{\rho} c_P^{\text{sat}}(1 - \text{RH}). \tag{4.18}$$

The next section will be dedicated to comparison of the quantitative parameters τ and L_g with experiments.

5. Comparison between experiments and theory

We now compare the predictions from the previous section with the data from figure 5.

First, we plot L_g^2/τ as a function of w, in figure 7*a*. From (4.18), all data should collapse onto a single horizontal line. We observe that it is indeed the case within 20%.

Second, we plot τ as a function of the geometrical parameter $hw/\tilde{q}_\ell$, in figure 7*b*. We use the values of $\tilde{q}_\ell$ for the experimental values of the geometrical parameters (figure 6). Equation (4.16) predicts that all data should collapse onto a single linear curve. Figure 7*b* shows that each series of data follows indeed such a linear trend, and that the slopes are similar, except the series for $h = 75\,\mu\text{m}$ which shows a slightly lower slope.

Third, we plot L_g as a function of the geometrical parameter $\sqrt{hw/\tilde{q}_\ell}$. Equation (4.17) predicts that all data should collapse onto a single linear curve. Figure 7*c* shows that this is the case in good approximation for all series.

The mean of the data is $\langle L_g^2/\tau \rangle = 8.6 \times 10^{-10}\,\text{m}^2\,\text{s}^{-1}$ (figure 7*a*). Now, $D_a M/\rho = 5.0 \times 10^{-10}\,\text{mol (m s)}^{-1}$. If we take $\alpha = 0.03$ from the estimate made in §4.3, $c_P^{\text{sat}} = 40\,\text{mol m}^{-3}$ from Randall & Doyle [28], and $c_a^{\text{out}} = 0$, we then have the prediction $L_g^2/\tau = \alpha D_a M c_P^{\text{sat}}(1 - \text{RH})/\rho = 6 \times 10^{-10}\,\text{m}^2\,\text{s}^{-1}$, in good agreement with our experimental value of $\langle L_g^2/\tau \rangle$.

The linear fit $\tau = c_\tau hw/\tilde{q}_\ell$ yields $c_\tau = 0.91\,\text{s}\,\mu\text{m}^{-2}$ as best-fitting parameter (figure 7*b*). This value must be compared to $\rho/[2D_P M c_P^{\text{sat}}(1 - \text{RH})]$; see prediction (4.16). If we use $D_P = 10^{-9}\,\text{m}^2\,\text{s}^{-1}$, we compute $\rho/[2D_P M c_P^{\text{sat}}(1 - \text{RH})] = 0.7\,\text{s}\,\mu\text{m}^{-2}$, once again in good agreement with experiments. The linear fit $L_g = c_{L_g}\sqrt{hw/\tilde{q}_\ell}$ yields $c_{L_g} = 27$ as best-fitting parameter (figure 7*c*). This value must be compared to $\sqrt{\alpha D_a/2D_P}$; see prediction (4.17). If we use $\alpha = 0.03$ and $D_P = 10^{-9}\,\text{m}^2\,\text{s}^{-1}$, we compute $\sqrt{\alpha D_a/2D_P} = 20$, once again in good agreement with experiments. We can conclude that our model captures quantitatively the drying dynamics with good accuracy, without adjustable parameters. The main source of uncertainty is likely PDMS ageing, even though we took care to perform experiments within 1 day after the preparation of our PDMS samples. Indeed, the reticulation of PDMS with its curing agent is a slowly ongoing reaction, which probably makes quantities such as c_P^{sat}, α and D_P drift over time.

Finally, our analysis enables us to explain why at given thicknesses, the wider the channel, the slower the drying process. Substituting (4.13) in (4.16) indeed yields

$$\tau = \frac{\rho h}{D_P M c_P^{\text{sat}}(1 - \text{RH})}\left\{\frac{1}{\delta} + \frac{4}{w}\left[\ln\frac{(H + \delta)h}{\delta^2} + \frac{H}{\delta}\ln\frac{H + \delta}{h}\right]\right\}^{-1}, \tag{5.1}$$

which is an increasing function of the channel width w, with a limit value $\lim_{w\to\infty} \tau = \rho h/[D_P M c_P^{\text{sat}}(1 - \text{RH})\delta]$. Narrow channels dry faster because of the side channel contribution which is independent of the channel width, and which thus becomes an increasingly efficient contribution to drying as the width decreases. This is clearly visible in a 'race' experiment such as the one of figure 3*b*. The physical explanation is the following: evaporation from narrow channels has a contribution from edges that is relatively more important compared to large channels.

We now discuss the applicability of our model, starting by evaluating the assumptions stated at the beginning of §4.1. First, channels can be considered as independent if they are separated by a distance larger than a few times the PDMS thickness H, which acts as a screening length for diffusion problems. If channels are closer or come as a bundle, their coupling must be included [15]. Second, as L_g is the distance from the

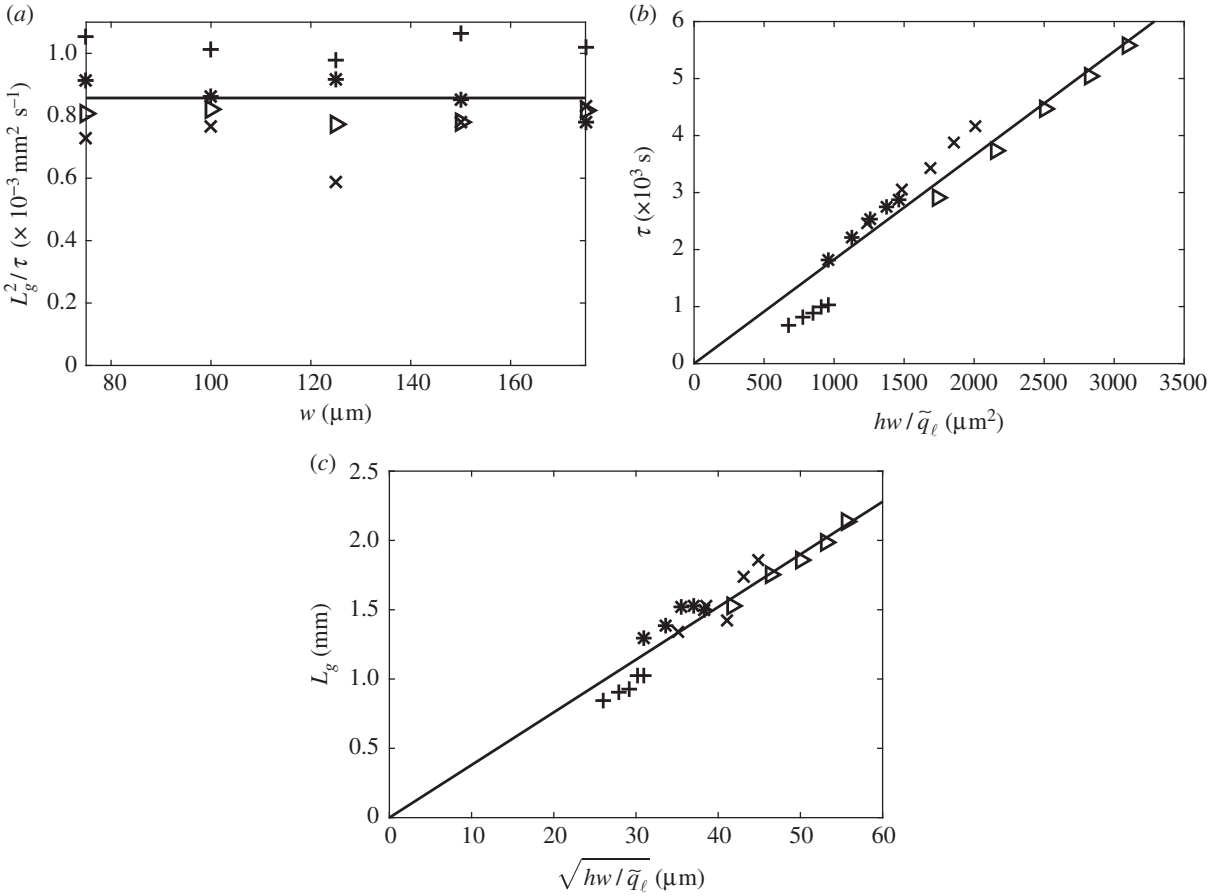

Figure 7. Comparison between experiments and model (see table 1 for the definition of symbols). (*a*) Plot of L_g^2/τ as a function of w. The horizontal line represents the mean of the data, $\langle L_g^2/\tau \rangle = 8.6 \times 10^{-10}$ m^2 s^{-1}. The standard deviation of the data is $\sigma_{L_g^2/\tau} = 1.2 \times 10^{-10}$ m^2 s^{-1}. (*b*) Plot of τ as a function of $hw/\tilde{q}_\ell$. The line is the best linear fit of the data. (*c*) Plot of L_g as a function of $\sqrt{hw/\tilde{q}_\ell}$. The line is the best linear fit of the data.

meniscus over which air within the channel dries, entrance effects, namely the influence of the open end of the channel, may be neglected as soon as the meniscus is at distances larger than L_g from the open end, which is true in our experiments. Moreover, we neglect pressure effects. In the present case, capillary pressures are much larger than viscous pressure drops. As the meniscus is curved, there is a Laplace pressure jump P_L of order γ/h across it, with $\gamma = 0.07$ N m^{-1} the surface tension; hence in our case, $P_L \approx 2$ kPa. This remains two orders of magnitude smaller than the ambient pressure, hence it does not significantly modify the saturation conditions in air and in PDMS. However, capillary underpressure in water may deform PDMS inwards the channel. To assess such an effect, we simulated with Matlab the elastic deformation of PDMS under the pressure difference $P_L = 2$ kPa in the most deformable case: the widest channel ($w = 175$ μm) and the thinnest PDMS cap ($\delta = 39$ μm), with a Young modulus $E = 2$ MPa and a bulk modulus $K = 1.5 \times 10^8$ Pa [30]. In this simulation, the maximal inward displacement, at the centre of the top channel–PDMS interface, did not exceed 1 μm, which is much lower than h: deformation is thus negligible. More generally, if $w > \delta$, the theory of plates may be used in the first approximation to get the following order of magnitude of the inward displacement: $P_L w^4/E\delta^3$, which must be compared to h to evaluate deformation effects. Furthermore, the model still holds for non-straight channels if the radius of curvature of their centreline is much larger than H, and for non-constant ambient conditions c_a^{out} if they vary over time scales much larger than the typical diffusion time H^2/D_P. We can also justify the quasi-steady diffusion assumption made in our model. It amounts to evaluating the ratio of time scales τ_{diff}/τ, where $\tau_{\text{diff}} \approx a^2/D_P$ with a the order of magnitude of h, w and H. From (5.1), we then obtain: $\tau_{\text{diff}}/\tau \approx Mc_P^{\text{sat}}/\rho$, up to a purely geometrical dimensionless prefactor of order one. Now, $Mc_P^{\text{sat}}/\rho = 10^{-3}$, hence $\tau_{\text{diff}}/\tau \ll 1$, which fully justifies the quasi-steady nature of water diffusion within PDMS, whatever the typical scale a.

Finally, and most crucially, our study is limited to isolated channels. Physically, this is the elementary building block towards understanding drying in the complex networks encountered in, for example, rocks or leaves, which show more complex dynamics owing to channel intercoupling [14]. The implications of channel–channel interactions will be the subject of an upcoming study.

6. Conclusion

Nature and technology's myriad drying processes make clear that the system drying kinetics depends on both its geometry and its scale. We have identified the dominant effects in an important special case: drying from a long channel embedded in a permeable medium. To complement the experiments, we have suggested a physical picture which highlights the importance of two effects. First, narrow channels dry relatively faster because transport through the side walls becomes increasingly important. This accentuates the relevance of including three-dimensional effects in analyses of drying. Second, the drying speed tends towards a constant, finite value at the end of drying, because of the evaporation from

the meniscus. These processes have been modelled by detailed analytical calculations. This allows us to rationalize experimental observations across a wide range of parameters, and our study sheds insight into the key parameters relevant to optimizing drying processes in engineering applications and to understand drying in the complex networks of real leaves.

Data accessibility. All data are available in the paper.

Authors' contributions. M.A., J.F.L. and B.D. carried out the laboratory work, B.D. and M.A. performed data analysis, B.D. developed the theoretical model, B.D. and P.M. designed and coordinated the study, B.D., J.F.L., K.H.J. and P.M. drafted the manuscript. All authors gave final approval for publication.

Competing interests. We declare we have no competing interests.

Funding. K.H.J. and J.F.L. were supported by a research grant (17587) from VILLUM FONDEN.

Acknowledgements. We thank Florie Mesple for the assistance with numerical simulations which have helped validating our analytical calculations. We thank Tim Brodribb, University of Tasmania, for providing equipment to photograph the grass leaf.

Appendix A. Analytical derivation of the flux $\tilde{q}_\ell$

We start by stating the dimensionless version of the problem to solve in §4.2. We define a dimensionless concentration $\tilde{c}_P = (c_P - c_a^{\text{out}}/\alpha)/(c_P^{\text{sat}} - c_a^{\text{out}}/\alpha)$, equal to 0 at the outer PDMS surface and to 1 at the channel/PDMS surface. We rescale lengths by the half-width $w/2$ of the channel, and thus define: $\tilde{x} = 2x/w$, $\tilde{y} = 2y/w$ and $\tilde{z} = 2z/w$. We thus have $\tilde{c}_P = f$, with f a solution of Laplace equation

$$\frac{\partial^2 f}{\partial \tilde{y}^2} + \frac{\partial^2 f}{\partial \tilde{z}^2} = 0, \tag{A 1}$$

with boundary conditions

$$\left.\begin{aligned} f &= 1 \text{ on } \mathcal{C}_{\text{channel}},\\ f &= 0 \text{ on } \mathcal{C}_{\text{out}},\\ \frac{\partial f}{\partial \tilde{z}} &= 0 \text{ on } \mathcal{C}_{\text{glass}}\\ \text{and}\quad \frac{\partial f}{\partial \tilde{y}} &= 0 \text{ on } \mathcal{C}_{\text{sym}}. \end{aligned}\right\} \tag{A 2}$$

Moreover, from (4.10) and (4.12), the flux to be computed equals

$$\tilde{q}_\ell = -2\int_0^\infty \left.\frac{\partial f}{\partial \tilde{z}}\right|_{\tilde{z}=\tilde{H}} \mathrm{d}\tilde{y}. \tag{A 3}$$

A.1. Two Schwarz–Christoffel transformations

The geometry of the channel cross section (figure 2*c*) is amenable to a standard technique of complex analysis: conformal mapping, and more precisely to Schwarz–Christoffel transformation, which maps the half-PDMS cross section (using the symmetry with respect to the $y = 0$ axis) onto the upper half-complex plane. This transformation takes the from [31]

$$z = C\int \prod_{i=1}^{4} (\zeta - \zeta_i)^{\alpha_i - 1}\,\mathrm{d}\zeta + D, \tag{A 4}$$

where $z = \tilde{y} + \mathrm{i}\tilde{z}$ is the complex variable describing the PDMS cross section (in this appendix A, z is not the vertical direction as in figure 2*b*,*c*), and $\zeta = \xi + \mathrm{i}\eta$ is the one

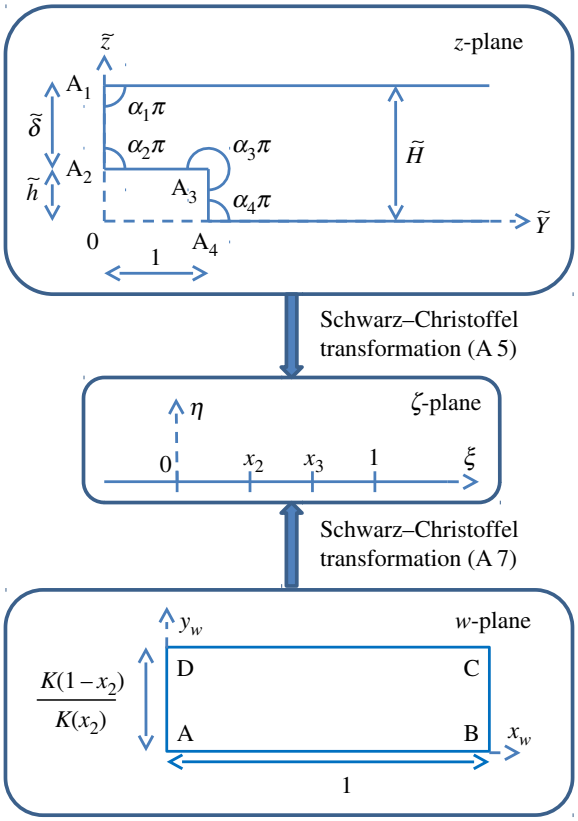

Figure 8. Schwarz–Christoffel transformations used to determine analytically the concentration field in the PDMS cross section. (Online version in colour.)

describing the upper half-complex plane onto which the PDMS cross section is mapped. In equation (A 4), the product corresponds to the four corners A_1, A_2, A_3 and A_4 of the original domain (figure 8), located, respectively, at $z_1 = \mathrm{i}\tilde{H}$, $z_2 = \mathrm{i}\tilde{h}$, $z_3 = 1 + \mathrm{i}\tilde{h}$ and $z_4 = 1$. The quantity α_i is related to the angles at these four corners: $\alpha_1 = \alpha_2 = \alpha_4 = 1/2$, and $\alpha_3 = 3/2$ (figure 8).

In equation (A 4), we have the freedom to ascribe the mapping of two points [31]. A possible choice consists in mapping A_1 to $\zeta = 0$, and A_4 to $\zeta = 1$. Equation (A 4) then becomes

$$z = C\int_0^\zeta \sqrt{\frac{\zeta' - x_3}{\zeta'(\zeta' - x_2)(\zeta' - 1)}}\,\mathrm{d}\zeta' + \mathrm{i}\tilde{H}. \tag{A 5}$$

With this choice, A_2 is mapped onto $\zeta = x_2$ and A_3 onto $\zeta = x_3$, with $0 < x_2 < x_3 < 1$. The two numbers x_2 and x_3, and the constant C, are then the solutions of the system of nonlinear equations

$$\tilde{H} - \tilde{h} = C\int_0^{x_2} \sqrt{\frac{x_3 - x}{x(x_2 - x)(1 - x)}}\,\mathrm{d}x,$$

$$1 = C\int_{x_2}^{x_3} \sqrt{\frac{x_3 - x}{x(x - x_2)(1 - x)}}\,\mathrm{d}x$$

and

$$\tilde{h} = C\int_{x_3}^{1} \sqrt{\frac{x - x_3}{x(x - x_2)(1 - x)}}\,\mathrm{d}x,$$

where the integrals can be expressed as functions of complete elliptic integrals. Combining these three equations and using formulae 3.167.19, 3.167.21 and 3.167.22 from Gradshteyn &

Ryzhik [32], we obtain

$$\left.\begin{aligned}\tilde{H}-\tilde{h}&=\tfrac{x_3-x_2}{1-x_3}\tfrac{\Pi(x_2/x_3,\,r)}{\Pi((x_3-x_2)/(1-x_2),\,q)-K(q)}\\ \text{and}\qquad \tilde{h}&=\tfrac{x_3-x_2}{1-x_3}\tfrac{\Pi((1-x_3)/(1-x_2),\,r)-K(r)}{\Pi((x_3-x_2)/(1-x_2),\,q)-K(q)},\end{aligned}\right\}\qquad (A\,6)$$

where $r=(1-x_3)x_2/[(1-x_2)x_3]$ and $q=(x_3-x_2)/[(1-x_2)x_3]$, and where K and Π are the complete elliptic integrals of the first and third kind, respectively, defined as

$$K(k)=\int_0^{\pi/2}\frac{\mathrm{d}t}{\sqrt{1-k\,\sin^2 t}}$$

and

$$\Pi(n,\,k)=\int_0^{\pi/2}\frac{\mathrm{d}t}{(1-n\,\sin^2 t)\sqrt{1-k\,\sin^2 t}}.$$

We can now use this transformation to solve Laplace equation (A 1) subject to boundary conditions (A 2). As Laplace equation is invariant under conformal mapping [31], the problem to solve in the upper half ζ-plane is, with $\zeta=\xi+\mathrm{i}\eta$: $\partial^2 f/\partial\xi^2+\partial^2 f/\partial\eta^2=0$, with boundary conditions on $\eta=0$: $f=0$ for $\xi\le 0$, $\partial f/\partial\eta=0$ for $0<\xi<x_2$ and for $\xi>1$, and $f=1$ for $x_2\le\xi\le x_3$.

Owing to the alternate nature of the boundary conditions, alternatively of the Dirichlet (imposed concentration) or Neumann (imposed flux) kind, there exists no direct solution of such a problem. To proceed, we use another Schwarz–Christoffel transformation, which maps the rectangle ABCD onto the ζ-plane, where A is located at $w=0$, B at $w=1$, and D at $w=\mathrm{i}d$, onto the upper half-complex plane, such that A is mapped to $\zeta=0$, B to $\zeta=x_2$, C to $\zeta=1$, and D to $\zeta=\pm\infty$ (figure 8). Such a transformation is written

$$w=C_w\int_0^{\zeta}\frac{\mathrm{d}\zeta'}{\sqrt{\zeta'(\zeta'-x_2)(\zeta'-1)}},\qquad (A\,7)$$

provided

$$1=w(\mathrm{B})-w(\mathrm{A})=C_w\int_0^{x_2}\frac{\mathrm{d}\xi}{\sqrt{\xi(x_2-\xi)(1-\xi)}}=2C_wK(x_2),$$

and

$$d=w(\mathrm{D})-w(\mathrm{A})=C_w\int_{-\infty}^{0}\frac{\mathrm{d}\xi}{\sqrt{-\xi(x_2-\xi)(1-\xi)}}=2C_wK(1-x_2).$$

These conditions impose

$$C_w=\frac{1}{2K(x_2)}\qquad (A\,8)$$

and $d=K(1-x_2)/K(x_2)$. Now, the problem to solve in the w-rectangle is, writing $w=x_w+\mathrm{i}y_w$: $\partial^2 f/\partial x_w^2+\partial^2 f/\partial y_w^2=0$, with boundary conditions: $f=0$ on DA, $\partial f/\partial y_w=0$ on AB and CD, and $f=1$ on BC. The solution is trivially $f=x_w$. In particular, the concentration gradient is unity along x_w

$$\frac{\partial f}{\partial x_w}=1\quad\text{and}\quad\frac{\partial f}{\partial y_w}=0.\qquad (A\,9)$$

A.2. Expression of the flux

We now use the two transformations (A 5) and (A 7) to express the flux $\tilde{q}_\ell$ in closed form. The transformation (A 5) can be considered as a change of variables from $(\tilde{y},\,\tilde{z})$ to $(\xi,\,\eta)$. Using the chain rule, we obtain

$$\frac{\partial f}{\partial\tilde{z}}(\tilde{y},\,\tilde{z})=\frac{\partial\xi}{\partial\tilde{z}}(\tilde{y},\,\tilde{z})\frac{\partial f}{\partial\xi}(\xi,\,\eta)+\frac{\partial\eta}{\partial\tilde{z}}(\tilde{y},\,\tilde{z})\frac{\partial f}{\partial\eta}(\xi,\,\eta).$$

In particular, if we specify this formula on the air/PDMS interface, $\tilde{z}=\tilde{H}$ and $\tilde{y}\ge 0$, this corresponds to the semi-axis $\eta=0$, $\xi\le 0$. Now from the Schwarz–Christoffel formula (A 5), $z'(\zeta)=C\sqrt{(\zeta-x_3)/[\zeta(\zeta-x_2)(\zeta-1)]}$, hence on the semi-axis $\eta=0$, $\xi\le 0$: $\partial\tilde{y}/\partial\xi=0$ and $\partial\tilde{y}/\partial\eta=C\sqrt{(x_3-\xi)/[-\xi(x_2-\xi)(1-\xi)]}$. Therefore,

$$\frac{\partial f}{\partial\tilde{z}}(\tilde{y},\,\tilde{z}=\tilde{H})=\frac{1}{C}\sqrt{\frac{-\xi(x_2-\xi)(1-\xi)}{x_3-\xi}}\frac{\partial f}{\partial\eta}(\xi,\,\eta=0).\qquad (A\,10)$$

Similarly,

$$\frac{\partial f}{\partial\eta}(\eta,\,\xi)=\frac{\partial x_w}{\partial\eta}(\eta,\,\xi)\frac{\partial f}{\partial x_w}(x_w,\,y_w)+\frac{\partial y_w}{\partial\eta}(\eta,\,\xi)\frac{\partial f}{\partial y_w}(x_w,\,y_w),$$

hence from (A 9),

$$\frac{\partial f}{\partial\eta}(\eta,\,\xi)=\frac{\partial x_w}{\partial\eta}(\eta,\,\xi).\qquad (A\,11)$$

In particular, if we specify this formula on the semi-axis $\eta=0$, $\xi\le 0$, this corresponds to the interval DA in the w-plane. Now from the Schwarz–Christoffel formula (A 7) and the condition (A 8), $w'(\zeta)=1/[2K(x_2)\sqrt{\zeta(\zeta-x_2)(\zeta-1)}]$, hence specifying this formula on DA, (A 11) becomes

$$\frac{\partial f}{\partial\eta}(\eta=0,\,\xi)=-\frac{1}{2K(x_2)\sqrt{-\xi(x_2-\xi)(1-\xi)}}.$$

Inserting this expression in (A 10) yields

$$\frac{\partial f}{\partial\tilde{z}}(\tilde{y},\,\tilde{z}=\tilde{H})=-\frac{1}{2CK(x_2)\sqrt{x_3-\xi}}.\qquad (A\,12)$$

We are now in a position to provide an analytical expression of the flux $\tilde{q}_\ell$. From (A 3) and (A 12), we obtain

$$\tilde{q}_\ell=\frac{1}{CK(x_2)}\int_0^{\infty}\frac{\mathrm{d}\tilde{y}}{\sqrt{x_3-\xi}}.$$

We perform the variable change $\tilde{y}$ to ξ. From the transformation (A 5) specified on the semi-axis $\eta=0$, $\xi\le 0$, $\partial\tilde{y}/\partial\xi=C\sqrt{(x_3-\xi)/[-\xi(x_2-\xi)(1-\xi)]}$, hence

$$\tilde{q}_\ell=\frac{1}{K(x_2)}\int_{-\infty}^{0}\frac{\mathrm{d}\xi}{\sqrt{-\xi(x_2-\xi)(1-\xi)}},$$

which yields the expression of the flux as a function of the sole parameter x_2:

$$\tilde{q}_\ell=\frac{2K(1-x_2)}{K(x_2)},\qquad (A\,13)$$

which constitutes the main result of our analysis. The corresponding flux is plotted as a function of x_2 in figure 9. It is a decreasing function of x_2, diverging at $x_2\to 0$ and such that $\tilde{q}_\ell(x_2=1)=0$.

Our analysis provides a prediction of the flux $\tilde{q}_\ell$ for any value of the geometrical parameters h, w and H; it suffices to solve the system (A 6) for x_2 and use (A 13). We plot the values of $\tilde{q}_\ell$ as a contour plot in the parameter space $(\tilde{\delta},\,\tilde{h})$ in figure 10.

It turns out that for our experimental range of the geometrical parameters, solving (A 6) yields values of x_2 much smaller than 1. It is therefore of practical interest to expand (A 6) for $x_2\ll 1$. Using the asymptotic expansions of the

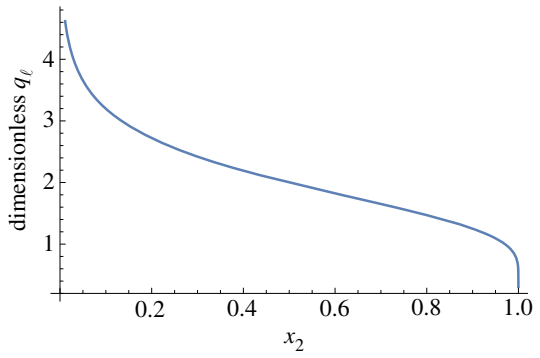

Figure 9. Plot of the flux as a function of the parameter x_2, from the expression (A 13). (Online version in colour.)

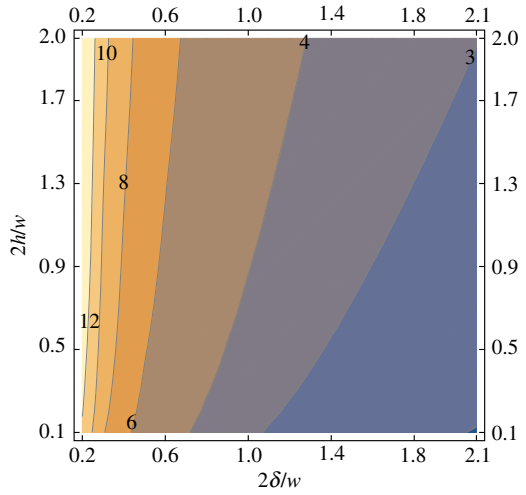

Figure 10. Contour plot of the flux as a function of the parameters $\tilde{\delta}$ and $\tilde{h}$, from the resolution of (A 6) and (A 13). Labels on the contour lines refer to the corresponding values of $\tilde{q}_\ell$ on these lines. (Online version in colour.)

complete elliptic integrals

$$\Pi(n,k)-K(k)=-\frac{n}{2(1-n)}\left[\ln(1-k)-4\ln 2+\frac{1}{\sqrt{n}}\ln\frac{1+\sqrt{n}}{1-\sqrt{n}}\right]+\mathcal{O}((1-k)\ln(1-k))$$

$$\text{and}\quad \Pi(n,k)=\frac{\pi}{2}\left(\frac{1}{\sqrt{1-n}}-1\right)+\mathcal{O}(n,k),\qquad K(k)=\frac{\pi}{2}+\mathcal{O}(k),$$

(A 6) becomes

$$\tilde{H}-\tilde{h}=-\pi\left[\ln x_2-4\ln 2+\ln\left(-1+\frac{1}{x_3}\right)+\frac{1}{\sqrt{x_3}}\ln\frac{1+\sqrt{x_3}}{1-\sqrt{x_3}}\right]^{-1}+\mathcal{O}(x_2\ln x_2)$$

$$\text{and}\quad \tilde{h}=-\pi\frac{1-\sqrt{x_3}}{\sqrt{x_3}}\left[\ln x_2-4\ln 2+\ln\left(-1+\frac{1}{x_3}\right)+\frac{1}{\sqrt{x_3}}\ln\frac{1+\sqrt{x_3}}{1-\sqrt{x_3}}\right]^{-1}+\mathcal{O}(x_2\ln x_2),$$

whence $\sqrt{x_3}=1-\tilde{h}/\tilde{H}+\mathcal{O}(x_2\ln x_2)$ and

$$\ln x_2-4\ln 2=-\frac{\pi}{\tilde{H}-\tilde{h}}-\ln\frac{(2\tilde{H}-\tilde{h})\tilde{h}}{(\tilde{H}-\tilde{h})^2}-\frac{\tilde{H}-\tilde{h}}{\tilde{H}}\ln\frac{2\tilde{H}-\tilde{h}}{\tilde{h}}+\mathcal{O}(x_2\ln x_2).\qquad\text{(A 14)}$$

This shows, in particular, that the approximation $x_2 \ll 1$ remains valid as long as $\tilde{H}-\tilde{h}$ does not get too large.

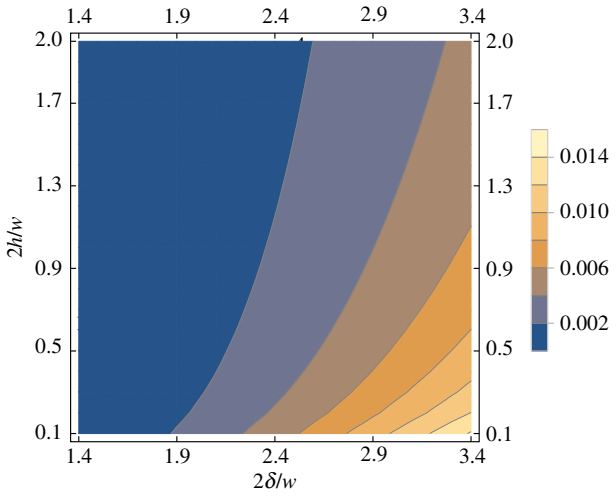

Figure 11. Contour plot of the relative error done when replacing the exact value of the flux, from the resolution of (A 6) and (A 13), by the approximation (4.13), as a function of the parameters $\tilde{\delta}$ and $\tilde{h}$. Note that the range of $\tilde{\delta}$ differs from figure 10; for any $\tilde{\delta} < 1.4$, the relative error is below 0.1%. (Online version in colour.)

Next, using the asymptotic expansions of the complete elliptic integral of first kind: $K(k)=\pi/2+\mathcal{O}(k)$ and $K(1-k)=-\frac{1}{2}\ln(1-k)+2\ln 2+\mathcal{O}((1-k)\ln(1-k))$, we obtain the expansion of (A 13): $\tilde{q}_\ell=-2(\ln x_2-4\ln 2)/\pi+\mathcal{O}(x_2\ln x_2)$. Using (A 14) and coming back to dimensional quantities, we obtain the explicit prediction (4.13) for the flux.

Finally, we compute the relative error done when replacing the exact value of the flux by the approximation (4.13). This relative error is shown as a contour plot in the parameter space $(\tilde{\delta},\tilde{h})$ in figure 11. This figure confirms the excellent accuracy of the approximation (4.13), as long as $\tilde{h}$ does not become much smaller than 1 and $\tilde{\delta}$ much larger than 1.

Appendix B. Analytical derivation of the flux Q_g

Like in appendix A, we start by stating the dimensionless version of the problem to solve in §4.3. We use the dimensionless variables defined in appendix A, plus the dimensionless concentration field in the channel: $\tilde{c}_a=(c_a-c_a^{\text{out}})/(c_a^{\text{sat}}-c_a^{\text{out}})$. We then have to solve, at $\tilde{x}>0$,

$$\frac{\partial^2\tilde{c}_i}{\partial\tilde{x}^2}+\frac{\partial^2\tilde{c}_i}{\partial\tilde{y}^2}+\frac{\partial^2\tilde{c}_i}{\partial\tilde{z}^2}=0,\qquad\text{(B 1)}$$

for $i=a,P$, with boundary conditions

$$\tilde{c}_P=0\ \text{on}\ \mathcal{C}_{\text{out}},\qquad\text{(B 2a)}$$

$$\frac{\partial\tilde{c}_P}{\partial\tilde{z}}=0\ \text{on}\ \mathcal{C}_{\text{glass}},\qquad\text{(B 2b)}$$

$$\frac{\partial\tilde{c}_a}{\partial\tilde{z}}=0\ \text{at}\ 0\le\tilde{y}\le 1\ \text{and}\ \tilde{z}=0,\qquad\text{(B 2c)}$$

$$\frac{\partial\tilde{c}_P}{\partial\tilde{y}}=0\ \text{on}\ \mathcal{C}_{\text{sym}},\qquad\text{(B 2d)}$$

$$\frac{\partial\tilde{c}_a}{\partial\tilde{y}}=0\ \text{at}\ \tilde{y}=0\ \text{and}\ 0\le\tilde{z}\le\tilde{h},\qquad\text{(B 2e)}$$

$$\tilde{c}_a=\tilde{c}_P\ \text{and}\ \nabla\tilde{c}_a\cdot\mathbf{n}=\epsilon\nabla\tilde{c}_P\cdot\mathbf{n}\ \text{on}\ \mathcal{C}_{\text{channel}},\qquad\text{(B 2f)}$$

$$\tilde{c}_a=1\ \text{at}\ \tilde{x}=0,\quad 0\le\tilde{y}\le 1\ \text{and}\ 0\le\tilde{z}\le\tilde{h}\qquad\text{(B 2g)}$$

$$\text{and}\qquad\lim_{\tilde{x}\to\infty}\tilde{c}_a=\lim_{\tilde{x}\to\infty}\tilde{c}_P=0,\qquad\text{(B 2h)}$$

where

$$\epsilon = \frac{D_P}{D_a}\frac{c_P^{\mathrm{sat}} - c_a^{\mathrm{out}}/\alpha}{c_a^{\mathrm{sat}} - c_a^{\mathrm{out}}} = \frac{D_P}{\alpha D_a}, \tag{B 3}$$

since α is estimated as $\alpha = c_a^{\mathrm{sat}}/c_P^{\mathrm{sat}}$; see §4.2.

As $D_a = 3 \times 10^{-5}\,\mathrm{m^2\,s^{-1}}$ and $D_P \approx 10^{-9}\,\mathrm{m^2\,s^{-1}}$ [27], using $\alpha = 0.03$, we compute $\varepsilon = 10^{-3}$. Hence, $\varepsilon \ll 1$, and we can solve the problem using perturbation methods. However, at leading order $\varepsilon = 0$, equation (B 2*f*) shows that PDMS becomes impermeable to water. This is incompatible with the boundary conditions at $\tilde{x} = 0$ and at $\tilde{x} \to \infty$, which express the progressive drying of the air within the channel as the distance to the meniscus increases. This suggests that $\tilde{x}$ must be rescaled is order to account for the channel/PDMS exchanges. Therefore, we pose the following expansions:

$$\tilde{c}_i \sim c_i^{(0)}(\hat{x}, \tilde{y}, \tilde{z}) + \epsilon c_i^{(1)}(\hat{x}, \tilde{y}, \tilde{z}) + \cdots,$$

for $i = a, P$, where $\hat{x} = \epsilon^\beta \tilde{x}$ with β is a positive exponent to be determined. Substituting this expansion in Laplace equation (B 1) yields

$$\frac{\partial^2 c_i^{(0)}}{\partial \tilde{y}^2} + \frac{\partial^2 c_i^{(0)}}{\partial \tilde{z}^2} + \epsilon\left(\frac{\partial^2 c_i^{(1)}}{\partial \tilde{y}^2} + \frac{\partial^2 c_i^{(1)}}{\partial \tilde{z}^2}\right) + \cdots + \epsilon^{2\beta}\frac{\partial^2 c_i^{(0)}}{\partial \hat{x}^2} + \cdots = 0. \tag{B 4}$$

Hence, at leading order, this equation and the boundary conditions (B 2) become

$$\frac{\partial^2 c_i^{(0)}}{\partial \tilde{y}^2} + \frac{\partial^2 c_i^{(0)}}{\partial \tilde{z}^2} = 0, \tag{B 5a}$$

$$c_P^{(0)} = 0 \text{ on } \mathcal{C}_{\mathrm{out}}, \tag{B 5b}$$

$$\frac{\partial c_P^{(0)}}{\partial \tilde{z}} = 0 \text{ on } \mathcal{C}_{\mathrm{glass}}, \tag{B 5c}$$

$$\frac{\partial c_a^{(0)}}{\partial \tilde{z}} = 0 \text{ at } 0 \le \tilde{y} \le 1 \text{ and } \tilde{z} = 0, \tag{B 5d}$$

$$\frac{\partial c_P^{(0)}}{\partial \tilde{y}} = 0 \text{ on } \mathcal{C}_{\mathrm{sym}}, \tag{B 5e}$$

$$\frac{\partial c_a^{(0)}}{\partial \tilde{y}} = 0 \text{ at } \tilde{y} = 0 \text{ and } 0 \le \tilde{z} \le \tilde{h}, \tag{B 5f}$$

$$c_a^{(0)} = c_P^{(0)} \text{ and } \nabla c_a^{(0)} \cdot \mathbf{n} = 0 \text{ on } \mathcal{C}_{\mathrm{channel}}, \tag{B 5g}$$

$$c_a^{(0)} = 1 \text{ at } \tilde{x} = 0, \quad 0 \le \tilde{y} \le 1 \text{ and } 0 \le \tilde{z} \le \tilde{h} \tag{B 5h}$$

and

$$\lim_{\tilde{x}\to\infty} c_a^{(0)} = \lim_{\tilde{x}\to\infty} c_P^{(0)} = 0. \tag{B 5i}$$

The concentration field $c_a^{(0)}$ is subject to no-flux boundary conditions (B 5*d*), (B 5*f*) and (B 5*g*) all around the channel spanwise cross section. Hence, by property of Laplace equation, it does not depend on $\tilde{y}$ and $\tilde{z}$: $c_a^{(0)}(\tilde{y}, \hat{x}, \tilde{z}) = c_0(\hat{x})$ with c_0 a yet unknown function, which will be determined at order one. Then, if we define a new dimensionless concentration $\hat{c}_P = c_P/c_0$, $\hat{c}_P$ obeys exactly the boundary conditions (A 2), hence we have simply: $\hat{c}_P = f$, and

$$c_P^{(0)}(\hat{x}, \tilde{y}, \tilde{z}) = c_0(\hat{x}) f(\tilde{y}, \tilde{z}). \tag{B 6}$$

In particular, the evaporative flux per unit length along x is: $-2\int_0^\infty \partial c_P^{(0)}/\partial \tilde{z}|_{\tilde{z}=\tilde{H}}\,\mathrm{d}\tilde{y} = c_0 \tilde{q}_\ell$.

At the next order, the role of the streamwise direction x must appear. Hence from (B 4), we must set $\beta = 1/2$, and we have

$$\frac{\partial^2 c_a^{(1)}}{\partial \tilde{y}^2} + \frac{\partial^2 c_a^{(1)}}{\partial \tilde{z}^2} + \frac{\mathrm{d}^2 c_0}{\mathrm{d}\hat{x}^2} = 0, \tag{B 7}$$

with boundary conditions

$$\frac{\partial c_a^{(1)}}{\partial \tilde{z}} = 0 \text{ at } 0 \le \tilde{y} \le 1 \text{ and } \tilde{z} = 0, \tag{B 8a}$$

$$\frac{\partial c_a^{(1)}}{\partial \tilde{y}} = 0 \text{ at } \tilde{y} = 0 \text{ and } 0 \le \tilde{z} \le \tilde{h}, \tag{B 8b}$$

$$\frac{\partial c_a^{(1)}}{\partial \tilde{z}} = c_0 \frac{\partial f}{\partial \tilde{z}} \text{ at } 0 \le \tilde{y} \le 1 \text{ and } \tilde{z} = \tilde{h}, \tag{B 8c}$$

$$\frac{\partial c_a^{(1)}}{\partial \tilde{y}} = c_0 \frac{\partial f}{\partial \tilde{y}} \text{ at } \tilde{y} = 1 \text{ and } 0 \le \tilde{z} \le \tilde{h}, \tag{B 8d}$$

$$c_a^{(1)} = 1 \text{ at } \hat{x} = 0, \quad 0 \le \tilde{y} \le 1 \text{ and } 0 \le \tilde{z} \le \tilde{h} \tag{B 8e}$$

and

$$\lim_{\hat{x}\to\infty} c_a^{(1)} = 0. \tag{B 8f}$$

Hence, $c_a^{(1)}$ obeys Poisson equation with Neumann boundary conditions. The solution of such a problem is not unique, because it is known up to an arbitrary offset, but we shall see that it is of no importance when determining c_0. Solving such an equation analytically is standard [31]. We pose the Fourier series

$$\frac{\partial^2 c_a^{(1)}}{\partial \tilde{y}^2} = \frac{1}{2}a_0(\tilde{z}) + \sum_{n=1}^{\infty} a_n(\tilde{z}) \cos n\pi\tilde{y},$$

and

$$c_a^{(1)} = \frac{1}{2}A_0(\tilde{z}) + \sum_{n=1}^{\infty} A_n(\tilde{z}) \cos n\pi\tilde{y},$$

where

$$a_n = 2\int_0^1 \frac{\partial^2 c_a^{(1)}}{\partial \tilde{y}^2} \cos n\pi\tilde{y}\,\mathrm{d}\tilde{y},\ A_n = 2\int_0^1 c_a^{(1)} \cos n\pi\tilde{y}\,\mathrm{d}\tilde{y}.$$

Integrating by parts the expression of a_n and accounting for (B 8*b*) and (B 8*d*), we obtain

$$a_n = 2(-1)^n c_0 \frac{\partial f}{\partial \tilde{y}}(\tilde{y} = 1, \tilde{z}) - \pi^2 n^2 A_n.$$

Inserting these relations in Poisson equation (B 7) yields

$$-\frac{\mathrm{d}^2 c_0}{\mathrm{d}\hat{x}^2} = c_0 \frac{\partial f}{\partial \tilde{y}}(\tilde{y} = 1, \tilde{z}) + \frac{1}{2}\frac{\mathrm{d}^2 A_0}{\mathrm{d}\tilde{z}^2} + \sum_{n=1}^{\infty}\left[2(-1)^n c_0 \frac{\partial f}{\partial \tilde{y}}(\tilde{y} = 1, \tilde{z}) + \frac{\mathrm{d}^2 A_n}{\mathrm{d}\tilde{z}^2} - \pi^2 n^2 A_n\right]\cos n\pi\tilde{y}.$$

From the orthogonality of the set of $\cos n\pi\tilde{y}$ in the interval $0 \le \tilde{y} \le 1$, we obtain

$$\frac{\mathrm{d}^2 A_0}{\mathrm{d}\tilde{z}^2} = -2\left[\frac{\mathrm{d}^2 c_0}{\mathrm{d}\hat{x}^2} + c_0 \frac{\partial f}{\partial \tilde{y}}(\tilde{y} = 1, \tilde{z})\right], \tag{B 9}$$

and, $\forall n \in \mathbb{N}^*$, $\frac{\mathrm{d}^2 A_n}{\mathrm{d}\tilde{z}^2} - \pi^2 n^2 A_n = 2(-1)^{n+1} c_0 \frac{\partial f}{\partial \tilde{y}}(\tilde{y} = 1, \tilde{z})$. From (B 8*a*), we obtain that $\forall n \in \mathbb{N}$,

$$\frac{\mathrm{d}A_n}{\mathrm{d}\tilde{z}}(\tilde{z} = 0) = 0, \tag{B 10}$$

and from (B 8*c*), $c_0(\partial f/\partial \tilde{z})(\tilde{y}, \tilde{z} = \tilde{h}) = \frac{1}{2}(\mathrm{d}A_0/\mathrm{d}\tilde{z})(\tilde{z} = \tilde{h}) + \sum_{n=1}^{\infty}(\mathrm{d}A_n/\mathrm{d}\tilde{z})(\tilde{z} = \tilde{h})\cos n\pi\tilde{y}$. Using once again the orthogonality of the set of $\cos n\pi\tilde{y}$ in the interval $0 \le \tilde{y} \le 1$, we obtain

$$\frac{\mathrm{d}A_0}{\mathrm{d}\tilde{z}}(\tilde{z} = \tilde{h}) = 2c_0 \int_0^1 \frac{\partial f}{\partial \tilde{z}}(\tilde{y}, \tilde{z} = \tilde{h})\mathrm{d}\tilde{y}. \tag{B 11}$$

Solving (B 9) with boundary conditions (B 10) and (B 11) yields the compatibility equation for c_0

$$\frac{\mathrm{d}^2 c_0}{\mathrm{d}\hat{x}^2} + \frac{c_0}{\tilde{h}}\left[\int_0^1 \frac{\partial f}{\partial \tilde{z}}(\tilde{y}, \tilde{z} = \tilde{h})\,\mathrm{d}\tilde{y} + \int_0^{\tilde{h}} \frac{\partial f}{\partial \tilde{y}}(\tilde{y} = 1, \tilde{z})\,\mathrm{d}\tilde{z}\right] = 0.$$

Now, by flux conservation,

$$\int_0^1 \frac{\partial f}{\partial \tilde{z}}(\tilde{y}, \tilde{z}=\tilde{h})\mathrm{d}\tilde{y} + \int_0^{\tilde{h}} \frac{\partial f}{\partial \tilde{y}}(\tilde{y}=1, \tilde{z})\mathrm{d}\tilde{z} = -\frac{1}{2}\tilde{q}_\ell,$$

hence

$$\frac{\mathrm{d}^2 c_0}{\mathrm{d}\hat{x}^2} + \frac{\tilde{q}_\ell}{2\tilde{h}} c_0 = 0.$$

The solution of this equation subjected to boundary conditions (B 8*e*) and (B 8*f*) is simply

$$c_0(\hat{x}) = \exp\left(-\hat{x}\sqrt{\frac{\tilde{q}_\ell}{2\tilde{h}}}\right), \tag{B 12}$$

which fully determines the solution at leading order.

We can now compute Q_g. From its definition (4.3), $Q_g = -2D_P \int_0^\infty \mathrm{d}x \int_0^\infty \mathrm{d}y (\partial c_P/\partial z)_{z=H}$. From (B 6) and the definitions of the dimensionless lengths,

$$Q_g = -\left(c_P^{\mathrm{sat}} - \frac{c_a^{\mathrm{out}}}{\alpha}\right) w\sqrt{\alpha D_a D_P} \int_0^\infty \frac{\partial f}{\partial \tilde{z}}(\tilde{y}, \tilde{z}=\tilde{h})\,\mathrm{d}\tilde{y} \times \int_0^\infty c_0(\hat{x})\,\mathrm{d}\hat{x},$$

at leading order. The first integral is $-\tilde{q}_\ell/2$ by definition, while the second is readily evaluated from (B 12), and equals $\sqrt{2\tilde{h}/\tilde{q}_\ell}$. This finally yields the expression (4.15) for Q_g, from which we can rewrite (B 12) in the form

$$c_0(\hat{x}) = \mathrm{e}^{-x/L_g}. \tag{B 13}$$

References

1. Sholl DS, Lively RP. 2016 Seven chemical separations to change the world. *Nature* **532**, 435–437. (doi:10.1038/532435a)
2. Campbell IB, Claridge GGC. 1987 *Antarctica: soils, weathering processes and environment*. Developments in Soil Science, vol. 16, pp. 97122. Amsterdam, The Netherlands: Elsevier Science.
3. Rodriguez-Navarro C, Doehne E. 1999 Salt weathering: influence of the evaporation rate, supersaturation and crystallization pattern. *Earth Surf. Process. Landforms* **24**, 191–209. (doi:10.1002/(ISSN)1096-9837)
4. Priestley CHB, Taylor RJ. 1972 On the assessment of surface heat flux and evaporation using large-scale parameters. *Mon. Weather Rev.* **100**, 81–92. (doi:10.1175/1520-0493(1972)100¡0081:OTAOSH¿2.3.CO;2)
5. Hunt EH. 1912 The regulation of body temperature in extremes of dry heat. *Epidemiol. Infect.* **12**, 479–488.
6. Wilking JN, Zaburdaev V, De Volder M, Losick R, Brenner MP, Weitz DA. 2013 Liquid transport facilitated by channels in *Bacillus subtilis* biofilms. *Proc. Natl Acad. Sci. USA* **110**, 848–852. (doi:10.1073/pnas.1216376110)
7. Choat B, Brodribb TJ, Brodersen CR, Duursma RA, López R, Medlyn BE. 2018 Triggers of tree mortality under drought. *Nature* **558**, 531–539. (doi:10.1038/s41586-018-0240-x)
8. Ting IP, Loomis WE. 1963 Diffusion through stomates. *Am. J. Bot.* **50**, 866–872. (doi:10.1002/ajb2.1963.50.issue-9)
9. Wheeler TD, Stroock AD. 2008 The transpiration of water at negative pressures in a synthetic tree. *Nature* **455**, 208–212. (doi:10.1038/nature07226)
10. Ponomarenko A, Vincent O, Pietriga A, Cochard H, Badel E, Marmottant P. 2014 Ultrasonic emissions reveal individual cavitation bubbles in water-stressed wood. *J. R. Soc. Interface* **11**, 20140480. (doi:10.1098/rsif.2014.0480)
11. Vincent O, Marmottant P, Quinto-Su PA, Ohl CD. 2012 Birth and growth of cavitation bubbles within water under tension confined in a simple synthetic tree. *Phys. Rev. Lett.* **108**, 184502. (doi:10.1103/PhysRevLett.108.184502)
12. Vincent O, Marmottant P, Gonzalez-Avila SR, Ando K, Ohl CD. 2014 The fast dynamics of cavitation bubbles within water confined in elastic solids. *Soft Matter* **10**, 1455–1461. (doi:10.1039/c3sm52697f)
13. Vincent O, Sessoms DA, Huber EJ, Guioth J, Stroock AD. 2014 Drying by cavitation and poroelastic relaxations in porous media with macroscopic pores connected by nanoscale throats. *Phys. Rev. Lett.* **113**, 134501. (doi:10.1103/PhysRevLett.113.134501)
14. Brodribb T, Bienaimé D, Marmottant P. 2016 Revealing catastrophic failure of leaf networks under stress. *Proc. Natl Acad. Sci. USA* **113**, 4865–4869. (doi:10.1073/pnas.1522569113)
15. Noblin X, Mahadevan L, Coomaraswamy IA, Weitz DA, Holbrook NM, Zwieniecki MA. 2008 Optimal vein density in artificial and real leaves. *Proc. Natl Acad. Sci. USA* **105**, 9140–9144. (doi:10.1073/pnas.0709194105)
16. Louf JF, Guéna G, Badel E, Forterre Y. 2017 Universal poroelastic mechanism for hydraulic signals in biomimetic and natural branches. *Proc. Natl Acad. Sci. USA* **114**, 11 034–11 039. (doi:10.1073/pnas.1707675114)
17. Comtet J, Jensen KH, Turgeon R, Stroock AD, Hosoi AE. 2017 Passive phloem loading and long-distance transport in a synthetic tree-on-a-chip. *Nature Plants* **3**, 17032. (doi:10.1038/nplants.2017.32)
18. Jerjen I, Poulikakos L, Plamondon M, Schetz P, Luethi T, Flisch A. 2015 Drying of porous asphalt concrete investigated by X-ray computed tomography. *Phys. Procedia* **69**, 451–456. (doi:10.1016/j.phpro.2015.07.063)
19. Walker GM, Beebe DJ. 2002 An evaporation-based microfluidic sample concentration method. *Lab Chip* **2**, 57–61. (doi:10.1039/b202473j)
20. Eijkel JCT, Bomer JG, van den Berg A. 2005 Osmosis and pervaporation in polyimide submicron microfluidic channel structures. *Appl. Phys. Lett.* **87**, 114103. (doi:10.1063/1.2046727)
21. Leng J, Lonetti B, Tabeling P, Joanicot M, Ajdari A. 2006 Microevaporators for kinetic exploration of phase diagrams. *Phys. Rev. Lett.* **96**, 084503. (doi:10.1103/PhysRevLett.96.084503)
22. Merlin A, Salmon JB, Leng J. 2012 Microfluidic-assisted growth of colloidal crystals. *Soft Matter* **8**, 3526–3537. (doi:10.1039/c2sm07149e)
23. Ziane N, Guirardel M, Leng J, Salmon JB. 2015 Drying with no concentration gradient in large microfluidic droplets. *Soft Matter* **11**, 3637–3642. (doi:10.1039/C5SM00299K)
24. Ziemecka I, Haut B, Scheid B. 2015 Hydrogen peroxide concentration by pervaporation of a ternary liquid solution in microfluidics. *Lab Chip* **15**, 504–511. (doi:10.1039/C4LC00886C)
25. Vincent O, Szenicer A, Stroock AD. 2016 Capillarity-driven flows at the continuum limit. *Soft Matter* **12**, 6656–6661. (doi:10.1039/C6SM00733C)
26. Volk A, Rossi M, Kähler CJ, Hilgenfeldt S, Marín A. 2015 Growth control of sessile microbubbles in PDMS devices. *Lab Chip* **15**, 4607–4613. (doi:10.1039/C5LC00982K)
27. Watson JM, Baron MG. 1996 The behaviour in water in poly(dimethylsiloxane). *J. Membr. Sci.* **110**, 47–57. (doi:10.1016/0376-7388(95)00229-4)
28. Randall GC, Doyle PS. 2005 Permeation-driven flow in poly(dimethylsiloxane) microfluidic devices. *Proc. Natl Acad. Sci. USA* **102**, 10 813–10 818. (doi:10.1073/pnas.0503287102)
29. Harley SJ, Glascoe EA, Maxwell RS. 2012 Thermodynamic study on dynamic water vapor sorption in Sylgard-184. *J. Phys. Chem. B* **116**, 14 183–14 190. (doi:10.1021/jp305997f)
30. Johnston ID, McCluskey DK, Tan CKL, Tracey MC. 2012 Mechanical characterization of bulk Sylgard 184 for microfluidics and microengineering. *J. Micromech. Microeng.* **24**, 035017. (doi:10.1088/0960-1317/24/3/035017)
31. Prosperetti A. 2011 *Advanced mathematics for applications*. Cambridge, UK: Cambridge University Press.
32. Gradshteyn IS, Ryzhik IM. 2007 *Table of integrals, series and products*, 7th edn. New York, NY: Academic Press.